


Measurement of fusion-evaporation cross sections for reactions of ^{44}Ca with $^{154,156,157,160}\text{Gd}$ targetsT. A. Werke,^{1,2,*} C. S. Salas,^{1,2,†} K. J. Glennon,^{1,2,‡} D. A. Mayorov,^{1,2,§} E. E. Tereshatov,¹
M. F. Volia,^{1,3,||} D. M. Wright,^{1,4,¶} and C. M. Folden, III^{1,2,#}¹*Cyclotron Institute, Texas A&M University, College Station, Texas 77843, USA*²*Department of Chemistry, Texas A&M University, College Station, Texas 77843, USA*³*Department of Nuclear Engineering, Texas A&M University, College Station, Texas 77843, USA*⁴*Department of Physics, University of Surrey, Guildford, Surrey GU2 7XH, United Kingdom* (Received 23 December 2020; revised 13 April 2022; accepted 29 June 2022; published 30 November 2022)

Background: Previously reported fusion-evaporation cross sections of residues in ^{45}Sc -induced reactions with lanthanide targets are much smaller than ^{48}Ca -induced reactions on the same targets. ^{44}Ca is one proton removed from ^{45}Sc and could be used to produce nuclei with a relative neutron content between those produced in the ^{45}Sc - and ^{48}Ca -induced reactions.

Purpose: Several experiments worldwide have attempted to discover elements beyond the currently heaviest known element, oganesson ($Z = 118$). Due to a lack of appropriate targets, these efforts focused on projectiles other than ^{48}Ca , which has been widely used for a number of successful element discovery experiments. The present study continues our previous work to understand the influence of various projectiles on the compound nucleus in fusion-evaporation reactions, and addresses the influence of target neutron number on fusion-evaporation cross sections.

Methods: In experiments performed at the Cyclotron Institute at Texas A&M University, a beam of $^{44}\text{Ca}^{6+}$ with an energy of $\approx 5\text{ MeV}/u$ was delivered by the K500 superconducting cyclotron to the Momentum Achromat Recoil Spectrometer (MARS). The ^{44}Ca projectiles bombarded various isotopically enriched Gd targets in the MARS target chamber to create evaporation residues, which were spatially separated from unreacted projectiles by MARS and identified via their characteristic α -decay energies. Excitation functions for the reactions of ^{44}Ca with $^{154,156,157,160}\text{Gd}$ were measured at several projectile energies each.

Results: The maximum $4n$ cross sections in the $^{44}\text{Ca} + ^{154,156,157,160}\text{Gd}$ reactions were 0.038 ± 0.008 , 0.83 ± 0.08 , 3.8 ± 0.2 , and 3.0 ± 0.5 mb, respectively. Production cross sections for the more neutron-rich targets were surprisingly constant even given the substantial changes in the difference in neutron binding energy and fission barrier of the compound nuclei.

Conclusions: Collective enhancements to level density caused a reduction in compound nucleus survivability for all targets. While this effect was required to obtain good agreement between theoretical calculations and experimental data, it was not sufficient to explain the cross sections for the reaction with the most neutron-deficient target studied (^{154}Gd). Instead, it appears that the difference in the fission barrier and neutron binding energy is the dominant factor affecting the survival of the compound nucleus in this case.

DOI: [10.1103/PhysRevC.106.054615](https://doi.org/10.1103/PhysRevC.106.054615)**I. INTRODUCTION**

Currently, 118 elements have been discovered and confirmed [1,2], and the experiments that discovered elements 114–118 all used ^{48}Ca projectiles as reviewed in [3]. Several additional experiments have been conducted as attempts to produce even heavier elements [4–9]. Due to the lack of appropriate targets heavier than ^{249}Cf , these experiments have relied on projectiles heavier than ^{48}Ca . Although these experiments have been highly sensitive and have reported small upper limit cross sections, the current authors are not aware of any reported decay chains indicative of elements with $Z > 118$ that are widely accepted by the community. The small cross sections for these and similar reactions have been attributed to the low survival probability of the compound nucleus (CN) [3,7,10]. This has been attributed to a

*Present address: Rock Island Arsenal, Rock Island, Illinois 61201, USA.

†Present address: Exflur Research Corporation, Round Rock, Texas 78665, USA.

‡Present address: Lawrence Livermore National Laboratory, Livermore, California 94550, USA.

§Present address: Institute for Defense Analyses, Alexandria, Virginia 22311, USA.

||Present address: Badan Pengawas Tenaga Nuklir, Jakarta Pusat 10120, Indonesia.

¶Present address: Atomic Weapons Establishment, Aldermaston, Reading, Berkshire RG7 4PR, United Kingdom.

#Folden@comp.tamu.edu

strong influence of survival probability on the average difference in fission barrier (B_f) and neutron binding energy (S_n) of the compound nucleus [11], represented as $B_f - S_n$. In a previous series of studies [12–15], our group systematically investigated the influence of heavy-ion projectiles on the fusion-evaporation cross section and observed this same effect. Additionally, we observed that collective enhancement to level density (CELD) (see, for example, [16] and references therein) has a significant impact on the production of the spherical evaporation residues (EvRs), which were generally near doubly magic ^{208}Pb . CELD causes a substantial increase in the level density as a heavy nucleus deforms slightly, due to high-lying rotational and vibrational states descending below the available excitation energy. The increased level density can increase the probability of fission and reduce the EvR cross sections.

Our previous paper included a systematic study of EvR cross sections for ^{44}Ca projectiles reacting with lanthanide targets of varying Z [12]. The current article expands the previous work by studying the influence of target neutron number while continuing to use ^{44}Ca as a projectile. The resulting CNs also have a range of deformations, which allows for the influence of deformation on CELD to be investigated. The latter effect is important, since the current authors are not aware of any measurements of the deformation of superheavy elements, and the impact of CELD on future element discovery experiments is not fully understood.

II. EXPERIMENT

Experiments were performed at the Cyclotron Institute at Texas A&M University. Source material of >95.90% enriched ^{44}Ca (chemical form ^{44}CaO , IsoFlex, San Francisco, California, USA) was heated in a high-temperature oven, and the evaporated atoms were injected into an electron cyclotron resonance (ECR) ion source. The ECR ion source ionized the ^{44}Ca to the $6+$ charge state, and the ions were subsequently injected into the K500 superconducting cyclotron. The primary beam of $^{44}\text{Ca}^{6+}$ was accelerated and directed to the target chamber of the Momentum Achromat Recoil Spectrometer (MARS) [13,17,18]. Two primary beam energies were used in the experiment; initially, the cyclotron produced a laboratory-frame beam energy of 214.3 MeV. Later, the beam energy was increased to 229.7 MeV to study the $^{44}\text{Ca} + ^{154}\text{Gd}$ excitation function. The uncertainty in the beam energy was $\approx 1\%$.

A schematic of MARS is presented in Fig. 1. Upon entering the target chamber, the beam first passed through a ^{nat}Al degrader, which reduced the beam energy. The beam then bombarded the target of interest, where the fusion-evaporation reaction occurred to create the EvR. The newly created EvRs passed through a $50\ \mu\text{g}/\text{cm}^2$ ^{nat}C stripper foil and entered the first quadrupole magnet, Q1. The majority of scattering products and other extraneous reaction products were spatially separated by the achromatic section of MARS between dipole magnets D1 and D2. The more rigid unreacted beam primarily deposited in the beam dump. Secondary separation of the EvRs occurred in the Wien filter. After passing through the separating elements, the EvRs were focused into the detector chamber, where they implanted into a position sensitive

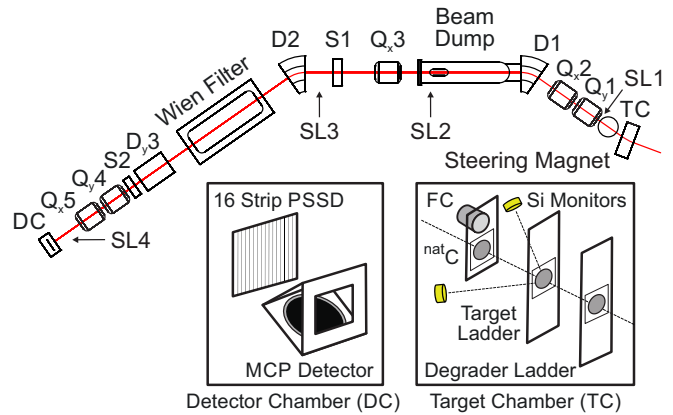


FIG. 1. MARS schematic with insets showing the detector chamber and the target chamber. Quadrupole, dipole, and sextupole magnets are labeled as Q, D, and S, respectively. The slits (SL2) at the downstream end of the Beam Dump define the momentum acceptance of MARS.

silicon detector (PSSD) (model X1, Micron Semiconductor Ltd., Lansing, UK) located at the focal plane. Finally, α -decaying EvRs were identified by their characteristic energies as measured by the PSSD.

Reactions of ^{44}Ca projectiles with targets of $^{160}\text{Gd}_2\text{O}_3$, $^{157}\text{Gd}_2\text{O}_3$, $^{156}\text{Gd}_2\text{O}_3$, and $^{154}\text{Gd}_2\text{O}_3$ were studied in the experiment. The targets were prepared in house using the molecular plating method [19–21]. Starting material for the $^{156}\text{Gd}_2\text{O}_3$ target was purchased from Isoflex as an oxide powder with an enrichment greater than 95.4%. Starting material for the other targets was obtained from the previous target-making group at the Cyclotron Institute. Approximately 1 mg of the starting material was dissolved in 0.1 or 2 M HNO_3 and evaporated to dryness under Ar gas. The resulting $\text{Gd}(\text{NO}_3)_3$ was reconstituted with 5–10 μL of 0.1 M HNO_3 and 12 mL of anhydrous isopropanol, and added to a custom electrodeposition cell [21,22]. The $\text{Gd}(\text{NO}_3)_3$ solution was plated onto a 2 μm Ti backing (Hamilton Precision Metals, Lancaster, Pennsylvania, USA) by applying a bias of 400–700 V for 30–60 min. The targets were baked at 200° C under atmospheric conditions to remove any volatile organic residues. The elemental composition of the targets was confirmed by energy-dispersive x-ray spectroscopy (EDS) as discussed in Ref. [21]. The isotopic composition of the targets was analyzed by laser ablation inductively coupled plasma mass spectrometry (LA-ICP-MS) and the results are given in Table I.

The MARS target chamber housed three motorized ladders, each remotely controllable via proprietary software. The most upstream ladder held one blank opening and a series of eight ^{nat}Al degraders used to reduce the beam energy. The nominal thicknesses of the degraders were 1.2, 1.8, 2.25, 2.85, 3.45, 4.5, 5.1, and 6.29 μm . These degrader thicknesses were selected to measure full excitation functions for the $4n$ exit channel for each of the four targets studied in this experiment. The middle ladder held the gadolinium oxide targets plus a check target of $334\ \mu\text{g}/\text{cm}^2$ $^{158}\text{Gd}_2\text{O}_3$ and thin foils of metallic ^{nat}Ta and ^{117}Sn . These three latter foils were used

TABLE I. Selected properties of reactions studied in this work. Target enrichment was measured using LA-ICP-MS. Beam dose was measured by the scattering detectors located in the target chamber as described in Sec. II.

Reaction	Compound nucleus	$\overline{B_f - S_n}$ (MeV)	Target enrichment (%)	Beam dose on target (10^{14})	MARS efficiency (%)
$^{44}\text{Ca} + ^{160}\text{Gd}$	^{204}Po	6.2	91.5	5.4	1.52
$^{44}\text{Ca} + ^{157}\text{Gd}$	^{201}Po	2.9	88.5	4.3	1.56
$^{44}\text{Ca} + ^{156}\text{Gd}$	^{200}Po	1.9	95.4	4.2	1.57
$^{44}\text{Ca} + ^{154}\text{Gd}$	^{198}Po	0.0	44.4 ^a	9.7	1.60

^aOther Gd nuclides present: ^{152}Gd (0.2%), ^{155}Gd (30.6%), ^{156}Gd (12.1%), ^{157}Gd (5.0%), ^{158}Gd (5.1%), and ^{160}Gd (2.6%).

for an efficiency calibration of the Rutherford scattering detectors as discussed below. The $^{158}\text{Gd}_2\text{O}_3$ target was used to check the MARS efficiency by comparing the EvR detection rate to previous studies done by our group [12]. The most downstream ladder held a phosphor-painted metal target with crosshairs used to visually view and align the beam spot, an electron-suppressed Faraday cup to measure the beam intensity inside the target chamber, and the $50 \mu\text{g}/\text{cm}^2$ $^{\text{nat}}\text{C}$ stripper foil.

The beam dose was measured via Coulomb scattering (also called ‘‘Rutherford’’ scattering) into two circular silicon detectors (model TU-015-150-300, ORTEC, Oak Ridge, Tennessee, USA) mounted at $\pm 30^\circ$ from the beam axis and 241 mm from the target. Detection efficiency was calibrated by inserting the targets of ^{117}Sn , $^{158}\text{Gd}_2\text{O}_3$, and $^{\text{nat}}\text{Ta}$ into the beam and measuring the scattered beam particles entering the detectors. A Faraday cup located near the extraction point of the cyclotron monitored the beam current and was used to normalize the effective solid angle of the scattering detectors. The electron-suppressed Faraday cup located in the target chamber was used to check the beam current in the target chamber and correct for beam current losses between the cyclotron and MARS. Total beam doses for the four targets studied in this experiment are listed in Table I.

The EvRs were tuned to the detector chamber of MARS (labeled ‘‘DC’’ in Fig. 1). The EvRs passed through a $2\text{-}\mu\text{m}$ Ti foil and ejected secondary electrons from the foil. These electrons were steered by an electrostatic potential onto a microchannel plate (MCP) detector (model APD2MA75/32/25/8D 40:1NR, Photonis USA, Sturbridge, Massachusetts). The EvRs then implanted in the PSSD, where they decayed. The MCP was used as a veto detector; an implanting EvR created a signal in both the MCP detector and the PSSD, while the decay of an implanted nuclide only created a signal in the PSSD. The veto was able to select the α particles with $>99\%$ efficiency. The efficiency of the PSSD for detecting the α particles was $(55 \pm 3)\%$. Typical resolution for α -particle peaks was 70–80 keV full width at half maximum.

The MARS efficiency was measured by inserting a $^{158}\text{Gd}_2\text{O}_3$ target and measuring the production of the ^{198}Po EvR in the $4n$ exit channel. This reaction was studied previously using MARS with a well-defined efficiency [12]. In this experiment, the center-of-target beam energy E_{CoT} of the ^{44}Ca on the ^{158}Gd target was 184.9 MeV. The ^{198}Po cross section was extrapolated from the measured excitation function [12] with three different linear fits to calculate the cross section of

1.88 mb. From the known ^{198}Po cross section σ_{EvR} , the MARS efficiency $\varepsilon_{\text{MARS}}$ was determined using Eq. (1):

$$\varepsilon_{\text{MARS}} = \frac{N_{\text{EvR, detected}}}{N_{\text{Ruth}}} \frac{1}{\sigma_{\text{EvR}}} \Omega_{\text{eff}} \frac{d\sigma_{\text{Ruth}}}{d\Omega} \frac{1}{\varepsilon_{\text{detect}} \varepsilon_{\alpha}}, \quad (1)$$

where $N_{\text{EvR, detected}}$ is the number of detected ^{198}Po EvRs from the measured α decay events, N_{Ruth} is the number of Rutherford scattering events detected, Ω_{eff} is the previously measured effective solid angle seen by the Rutherford scattering detectors, $d\sigma_{\text{Ruth}}/d\Omega$ is the known differential scattering cross section [23], $\varepsilon_{\text{detect}}$ is the PSSD α -particle detection efficiency, and ε_{α} is the α branching ratio of ^{198}Po . The MARS efficiency was measured for the ^{198}Po 19+, 20+, and 21+ charge states to ensure reproducibility, and the efficiency was periodically checked throughout the experiment. The MARS efficiencies for the four Gd isotopes studied in this experiment were adjusted by the mass asymmetry parameter $\eta = |A_p - A_t| / (A_p + A_t)$, as compared to the $^{44}\text{Ca} + ^{158}\text{Gd}$ reaction and calculated via a linear interpolation between the $^{40}\text{Ar} + ^{118}\text{Sn}$ and the $^{40}\text{Ar} + ^{165}\text{Ho}$ reactions [24,25]. MARS efficiencies for the reactions studied in this experiment are presented in Table I.

III. DATA ANALYSIS

Data analysis techniques were very similar to those described in our previous publications [12–15]. Regions of interest (ROIs) were identified for each EvR based on the characteristic α particle energy from the literature [26] and from the resolution of the PSSD. Example α particle spectra for each reaction are presented in Fig. 2. Each example spectrum corresponds to the peak of the $4n$ excitation function and the characteristic α energies are also noted. The LA-ICP-MS analysis showed that the ^{154}Gd target was not substantially enriched and contained other isotopes of gadolinium as shown in Table I. To account for possible contributions to the observed peaks from the other isotopes of gadolinium, model cross section calculations were performed for each possible contributing reaction [27]. The total contribution from each isotope to each peak was calculated by weighting the cross section and relative isotopic abundance in the ^{154}Gd target. The spurious contributions were then subtracted from the total counts from the observed peaks, leaving only the counts contributed by reactions with ^{154}Gd nuclei.

The identification of the EvRs was validated using an EvR- α time correlation analysis from the PSSD. The agreement between the measured half-lives in the current work and

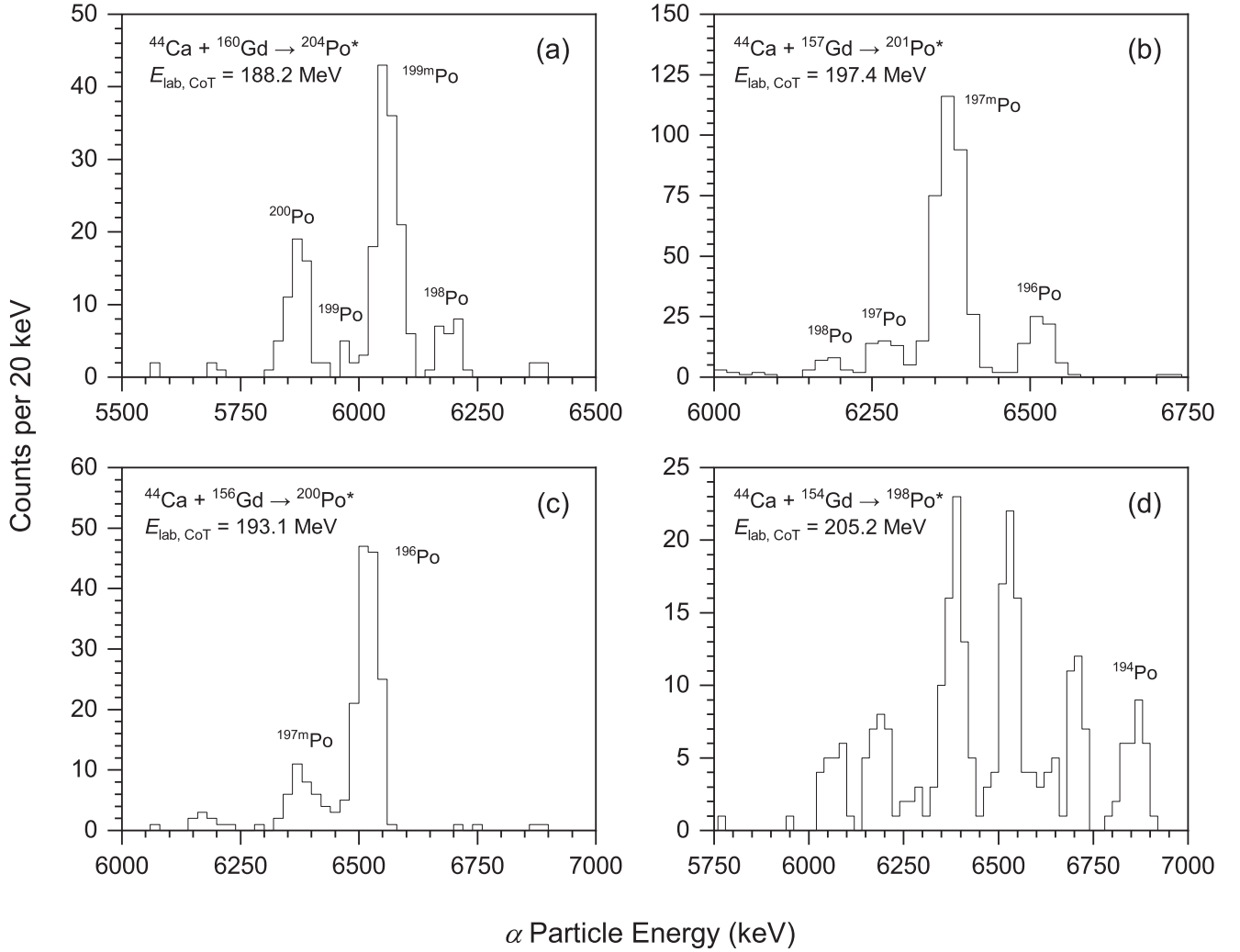


FIG. 2. Example α spectra observed in the indicated reactions. In panel (d), the unlabeled peaks are due to the additional Gd isotopes present in the ^{154}Gd target as listed in the footnote to Table I. The contributions of these nuclides to the relevant cross sections were subtracted as described in Sec. III.

previously reported half-lives [26] for the major xn channels is shown in Fig. 3. The line indicates exact agreement between previous reports and the current work and provides confidence that nuclide assignments in the current work are likely correct.

Each peak was fit and background-subtracted using the software package GF3 [28]. The number of counts for each EvR was extracted, and the cross section for each exit channel was calculated using Eq. (2):

$$\sigma_{\text{EvR}} = \frac{N_{\text{EvR,detect}}}{N_{\text{Ruth}}} \Omega_{\text{eff}} \frac{d\sigma_{\text{Ruth}}}{d\Omega} \frac{1}{\varepsilon_{\text{MARS}} \varepsilon_{\alpha} \varepsilon_{\text{PSSD}} \varepsilon_{\text{target}}}, \quad (2)$$

where $N_{\text{EvR,detect}}$ is the number of background-subtracted counts in the ROI, N_{Ruth} is the average number of Rutherford scattering counts measured, Ω_{eff} is the effective Rutherford scattering solid angle, $d\sigma_{\text{Ruth}}/d\Omega$ is the differential Rutherford scattering cross section [23], and the respective efficiencies, denoted by ε , are the MARS efficiency, α decay branching ratios [26], PSSD detection efficiency, and the isotopic enrichment of the target (see Table I).

The results were analyzed in the context of a theoretical model that has been described previously [12–15]. The key components of this model are three factors: the capture cross section σ_{cap} , the CN formation probability P_{CN} , and the probability of CN survival W_{sur} . First, the capture cross section is calculated using the “diffused barrier formula” proposed by Świątecki *et al.* [29] using Eqs. (2)–(8) in Ref. [15]. Next, the probability of CN formation was calculated using the semiempirical formula proposed by Siwek-Wilczyńska *et al.* [30] according to Eq. (3) in Ref. [13]. The “Jackson factor” P_{x_n} , which represents the probability of evaporating exactly x neutrons as opposed to some other number of neutrons, was calculated as described in [31]. Finally, the survival of the CN is calculated using the statistical formalism proposed by Siwek-Wilczyńska *et al.* [32] using Eqs. (4)–(20) in Ref. [13]. This involves estimating the various relevant decay widths using estimates of the level density parameter [33,34]. The angular-momentum-dependent liquid-drop fission barrier was estimated using the FISROT code [35,36], and the shell corrections to the fission barrier were taken from [37]. These data are

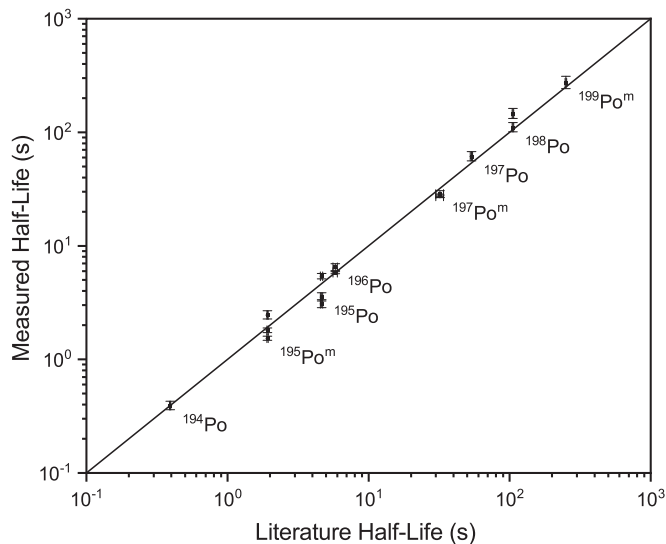


FIG. 3. Comparison of half-lives measured in the current work to those reported previously in Refs. [26,42]. The solid line indicates exact agreement between the two. Multiple data points for a given nuclide indicate separate measurements with different targets; these were not combined in order to look for systematic errors in temporally separated experiments. In some cases, the uncertainties are smaller than the data points.

summarized in Table II. Reduced charged particle emission barriers were applied as suggested by Parker *et al.* [38], but the resulting charged particle emission widths did not substantially affect the calculated cross sections. The influence of CELD [39] was also included. The latter are especially important and are affected by deformation. Notably, the calculated deformations of nuclei relevant to our experiment have changed substantially since our previous publications. Previously, we used the calculations of Möller *et al.* [40], but updated calculations by the same group are now available [37], and the newer data were used in the current work.

TABLE II. Shell correction energies to fission barriers [37] and angular-momentum-dependent liquid-drop fission barriers calculated using FISROT [35,36] for nuclides relevant to the current work. The total fission barrier was assumed to be the sum of the shell correction and the liquid-drop barrier for a given angular momentum. The liquid-drop values were calculated for all values of the angular momentum quantum number J from 0 to 30, but only a subset is shown for clarity.

Nuclide	Shell correction (MeV)	Liquid-drop fission barrier (MeV)						
		$J = 0$	$J = 5$	$J = 10$	$J = 15$	$J = 20$	$J = 25$	$J = 30$
^{204}Po	6.2	9.9	9.9	9.7	9.3	8.8	8.2	7.6
^{203}Po	5.5	9.8	9.7	9.5	9.1	8.7	8.1	7.4
^{202}Po	4.7	9.6	9.5	9.3	9.0	8.5	7.9	7.2
^{201}Po	3.5	9.4	9.3	9.1	8.8	8.3	7.7	7.0
^{200}Po	3.2	9.2	9.2	8.9	8.6	8.1	7.5	6.8
^{199}Po	2.1	9.0	9.0	8.7	8.4	7.9	7.3	6.7
^{198}Po	1.5	8.8	8.8	8.5	8.2	7.7	7.1	6.5
^{197}Po	0.9	8.6	8.5	8.3	8.0	7.5	6.9	6.2
^{196}Po	0.4	8.4	8.3	8.1	7.8	7.3	6.7	6.0
^{195}Po	0.0	8.2	8.1	7.9	7.5	7.1	6.5	5.8
^{194}Po	-0.3	8.0	7.9	7.7	7.3	6.8	6.3	5.6

IV. RESULTS AND DISCUSSION

Excitation functions for the $3n$ - $5n$ channels for reactions of $^{44}\text{Ca} + ^{154,156,157,160}\text{Gd}$ are shown in Fig. 4 since these were the main exit channels of interest in this work. A full listing of all measured EvR cross sections is also presented in Table III. Multiple neutron-emission exit channels were measured for each target, and this is discussed in detail below. No $p\alpha n$ exit channels were observed, and this is likely due to the small α -branching ratios (typically $< 1\%$, even for metastable states) for the Bi isotopes that would be produced in these reactions. All uncertainties presented in Table III are statistical only [41]. Due to the very small efficiency of MARS and the tendency for the magnetic fields to drift slightly throughout the experiment, the systematic uncertainty is estimated to be large (on the order of 50%).

In general, the fusion-evaporation cross sections vary as a function of target neutron richness in a way that is consistent with naïve expectations. The $^{160}\text{Gd}(^{44}\text{Ca}, xn)$ cross sections are generally the largest, as would be expected for a reaction with a relatively neutron-rich CN. The maximum cross section of any reaction was 8.7 ± 0.4 mb for the $^{160}\text{Gd}(^{44}\text{Ca}, 5n)$ reaction. This behavior is consistent with our previous measurements (see Fig. 7 in Ref. [12]), where larger cross sections were observed for reactions with more neutron-rich compound nuclei. The $^{156}\text{Gd}(^{44}\text{Ca}, 4n)$ cross sections are generally smaller by a factor of approximately 3–5 than those for the $^{160}\text{Gd}(^{44}\text{Ca}, 4n)$ reaction at a comparable excitation energy. The $^{154}\text{Gd}(^{44}\text{Ca}, 4n)$ cross sections are even smaller by an additional factor of ≈ 20 .

The agreement between the theoretical calculations and the experimental data is very good with differences generally less than an order of magnitude. However, the $3n$ product was not observed in the $^{44}\text{Ca} + ^{160}\text{Gd}$ reaction. The predicted cross sections for this reaction are actually *smaller* than for all other $3n$ reactions [see Fig. 4(a)], even though this is the most neutron-rich target in the current work. These low predictions are caused by small Jackson factors. For the relevant projectile energies, more than 14 MeV of excitation energy remains after

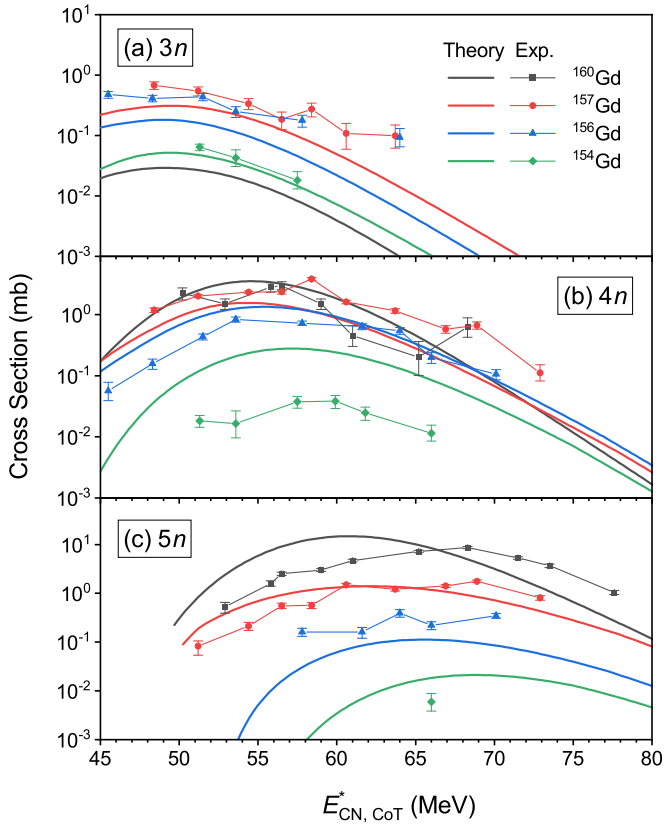


FIG. 4. Summary of calculated and measured cross sections for the (a) $3n$, (b) $4n$, and (c) $5n$ reactions in the current work as a function of excitation energy for compound nuclei formed at the center of the corresponding target $E_{\text{CN, CoT}}^*$. All three panels use the same symbols as indicated in panel (a). Heavy lines indicate theoretical calculations as described in Sec. III and symbols connected by thin lines represent experimental data. Not every exit channel was observed for each target. In some cases, the uncertainties are smaller than the symbols. The sharp cutoff in panel (c) for the theoretical calculations is due to the threshold energy; this was slightly higher than the nominal threshold energy because our model requires that each neutron carries away a kinetic energy equal to the nuclear temperature T . See the main text for additional discussion.

the emission of three neutrons. This is greater than the binding energy of the next neutron (7.65 MeV for ^{201}Po), so a fourth neutron emission is possible. For example, $P_{\text{xn}}(4n)/P_{\text{xn}}(3n)$ is estimated to be 9, 60, and 250 for CN excitation energies of 45, 50, and 55 MeV, respectively. In addition, our sensitivity for the $3n$ product was low (see below), so this exit channel was not observed.

The next largest discrepancy between experiment and theory was generally for the $4n$ channel in the $^{44}\text{Ca} + ^{154}\text{Gd}$ reaction. Here, the relatively high neutron binding energies are likely causing neutron emission to be suppressed to a greater extent than our calculations would suggest. The low survivability of the $^{44}\text{Ca} + ^{154}\text{Gd}$ deexcitation chain is confirmed in Fig. 5. This figure shows the sum of the measured xn channels (labeled $\Sigma\sigma_{xn}$ in the figure) for each reaction as an approximation of the total fusion-evaporation cross section, along with calculated values of σ_{cap} and $\sigma_{\text{cap}}P_{\text{CN}}$. The ratio of

$\Sigma\sigma_{xn}$ to $\sigma_{\text{cap}}P_{\text{CN}}$ gives a rough approximation of W_{sur} . This fraction is ≈ 0.6 for the ^{160}Gd target with $E_{\text{CoT}} = 180.1$ MeV, but decreases to $\approx 10^{-2}$ for $E_{\text{CoT}} = 215.0$ MeV. As expected, survival against fission is lower for each target with progressively fewer neutrons, and the smallest estimated value was $\approx 5 \times 10^{-5}$ for the ^{154}Gd target with the highest-energy projectiles. Overall, ^{154}Gd produced CN with the smallest survival probability against fission by far.

The ratio of $\sigma_{\text{cap}}P_{\text{CN}}$ to σ_{cap} in Fig. 5 gives our estimate of P_{CN} . In all cases, the values of P_{CN} for $E_{\text{CoT}} > 180$ MeV are greater than 0.08 and approach 1 with increasing E_{CoT} as expected for a system with a moderate value of $Z_{\text{p}}Z_{\text{t}}$ (1280).

The maximum $4n$ cross sections for the $^{44}\text{Ca} + ^{157,158,160}\text{Gd}$ reactions are surprisingly comparable. (The $^{44}\text{Ca} + ^{158}\text{Gd}$ reaction was studied in our previous work [12].) For all three targets, the CN and each neutron-emitting nucleus in the deexcitation chain have predicted quadrupole deformation parameters $|\beta_2| \leq 0.075$ [37]. Based on our previous research, we would expect these nearly spherical nuclei to have suppressed production cross sections due to CELD. This is confirmed by our theoretical calculations, which are shown in Fig. 6. The calculations require the inclusion of CELD in order to reproduce the experimental data. The discontinuity in the figure that appears at $\overline{B}_{\text{f}} - \overline{S}_{\text{n}} \approx 2$ MeV is an artifact that is caused by a large variation in cross section over a small variation in $\overline{B}_{\text{f}} - \overline{S}_{\text{n}}$ for the $^{44}\text{Ca} + ^{156}\text{Gd}$, ^{159}Tb , ^{162}Dy reactions. The cross sections decrease in the order of increasing target atomic number. This is primarily caused by a decrease in survival probability for higher atomic number targets, and to a lesser extent, a decrease in the fusion cross section.

In addition, Fig. 6 shows that relatively high values of $\overline{B}_{\text{f}} - \overline{S}_{\text{n}}$ (> 2.5 MeV) are necessary to maximize $4n$ cross sections. In contrast, the maximum $4n$ cross sections for the $^{44}\text{Ca} + ^{154,156}\text{Gd}$ reactions are smaller by factors of ≈ 80 and ≈ 3 , respectively. In these reactions, the deexcitation cascade progresses through nuclei with β_2 predicted to be as significant as -0.217 [37]. While our calculations suggest that CELD effects are present in these reactions, this does not completely explain the observed cross sections in the case of the $^{44}\text{Ca} + ^{154}\text{Gd}$ reaction. The low value of $\overline{B}_{\text{f}} - \overline{S}_{\text{n}}$ (≈ 0 MeV) appears to result in greater fission than expected and a $4n$ cross section even smaller than the predicted one. These results reinforce our previous conclusion that the primary influence on fusion-evaporation cross sections is the difference in the neutron binding energy and the fission barrier of the CN (see Ref. [12]).

Although our research was focused on excitation energies that were expected to be near the peak of the $4n$ excitation functions, a variety of exit channels was observed, including all channels from $4n-8n$ for the ^{160}Gd target. Production of the $3n$ product in this reaction seems possible, but our sensitivity for the $3n$ EvR (^{201}Po) was low due to its small α branches (1.1% for the ground state and 2.4% for the isomeric state [26]). The exit channel with the largest cross section for each target was $3n$, $4n$, $4n$, and $5n$ for the $^{154,156,157,160}\text{Gd}$ targets, respectively. These results are consistent with the interpretation that neutron emission is more likely in the more neutron-rich CN since neutron binding energies are smaller.

TABLE III. EvR cross sections for all measured exit channels in this experiment as a function of compound nucleus excitation energy at the center of the target $E_{\text{CN, CoT}}^*$. Uncertainties are statistical only and were calculated using the method of Schmidt *et al.* [41]. Asymmetric error bars are used when fewer than 20 counts were observed in the peak. Systematic errors are estimated to be $\pm 50\%$ due to the small efficiency of MARS and experimental uncertainties.

Reaction	$E_{\text{CN, CoT}}^*$ (MeV)	σ_{3n} (mb)	σ_{4n} (mb)	σ_{5n} (mb)	σ_{6n} (mb)	σ_{7n} (mb)	σ_{8n} (mb)
$^{44}\text{Ca} + ^{160}\text{Gd}$	50.2		2.2 ± 0.5				
	52.9		1.5 ± 0.3	0.52 ± 0.13			
	55.8		2.8 ± 0.5	1.6 ± 0.2	$0.094^{+0.045}_{-0.033}$		
	56.5		3.0 ± 0.5	2.5 ± 0.2	0.25 ± 0.07		
	59.0		1.5 ± 0.3	3.0 ± 0.2	0.21 ± 0.05	$0.039^{+0.022}_{-0.016}$	
	61.0		$0.45^{+0.21}_{-0.15}$	4.7 ± 0.3	0.21 ± 0.05	0.13 ± 0.03	
	65.2		$0.20^{+0.16}_{-0.10}$	7.2 ± 0.4	1.9 ± 0.2	0.21 ± 0.05	$0.035^{+0.022}_{-0.015}$
	68.3		$0.63^{+0.26}_{-0.20}$	8.7 ± 0.4	2.0 ± 0.2	0.30 ± 0.06	$0.060^{+0.029}_{-0.021}$
	71.5			5.3 ± 0.3	3.9 ± 0.2	0.23 ± 0.05	$0.056^{+0.027}_{-0.020}$
	73.5			3.7 ± 0.3	4.7 ± 0.3	0.25 ± 0.06	$0.071^{+0.029}_{-0.022}$
77.6			1.0 ± 0.1	4.5 ± 0.1	0.72 ± 0.05	0.066 ± 0.015	
$^{44}\text{Ca} + ^{157}\text{Gd}$	48.4	0.7 ± 0.1	1.2 ± 0.1				
	51.2	0.54 ± 0.09	2.0 ± 0.1	$0.083^{+0.029}_{-0.023}$			
	54.4	0.34 ± 0.07	2.3 ± 0.1	0.21 ± 0.04			
	56.5	0.19 ± 0.06	2.4 ± 0.2	0.55 ± 0.07			
	58.4	0.27 ± 0.07	3.8 ± 0.2	0.56 ± 0.08			
	60.6	0.11 ± 0.05	1.6 ± 0.1	1.5 ± 0.1			
	63.7	$0.099^{+0.051}_{-0.037}$	1.2 ± 0.1	1.2 ± 0.1			
	66.9		0.58 ± 0.08	1.4 ± 0.1			
	68.9		0.67 ± 0.09	1.8 ± 0.1	0.26 ± 0.06		
	72.9		$0.11^{+0.04}_{-0.03}$	0.81 ± 0.09	0.40 ± 0.07		
$^{44}\text{Ca} + ^{156}\text{Gd}$	45.5	0.48 ± 0.06	$0.056^{+0.022}_{-0.017}$				
	48.3	0.41 ± 0.05	0.16 ± 0.03				
	51.5	0.44 ± 0.06	0.43 ± 0.05				
	53.6	0.25 ± 0.05	0.83 ± 0.08				
	57.8	0.18 ± 0.04	0.73 ± 0.06	0.16 ± 0.03			
	61.6		0.64 ± 0.07	0.16 ± 0.04			
	64.0	$0.093^{+0.037}_{-0.028}$	0.55 ± 0.07	0.39 ± 0.07			
	66.0		0.20 ± 0.04	0.22 ± 0.04			
	70.1		0.11 ± 0.02	0.35 ± 0.04			
$^{44}\text{Ca} + ^{154}\text{Gd}$	51.3	0.064 ± 0.008	0.018 ± 0.004				
	53.6	$0.043^{+0.015}_{-0.012}$	$0.017^{+0.010}_{-0.007}$				
	57.5	$0.018^{+0.007}_{-0.005}$	0.038 ± 0.008				
	59.9		0.038 ± 0.009				
	61.8		0.025 ± 0.006				
	66.0		$0.012^{+0.004}_{-0.003}$	$0.0060^{+0.0029}_{-0.0021}$			

For example, the peak cross section for the $^{160}\text{Gd}(^{44}\text{Ca}, 4n)$ reaction occurs when the excitation energy is 56.5 MeV. However, only $\approx 52\%$ of the total xn cross section is observed in the $4n$ channel. This likely explains the surprising observation that the $^{157}\text{Gd}(^{44}\text{Ca}, 4n)$ cross sections are comparable in magnitude to the $^{160}\text{Gd}(^{44}\text{Ca}, 4n)$ cross sections. (The maximum cross sections are 3.8 ± 0.2 mb and 3.0 ± 0.5 mb, respectively.) The three additional neutrons provided by ^{160}Gd should result in an increase in W_{sur} , but much of this increase is contributing to the other, higher exit channels. In contrast, the peak cross section of the $^{157}\text{Gd}(^{44}\text{Ca}, 4n)$ reaction occurs when the excitation energy is 58.4 MeV, and under these conditions, $\approx 82\%$ of the total xn cross section is contributing to the $4n$ exit channel. For comparison, the peak cross section

of the $^{156}\text{Gd}(^{44}\text{Ca}, 4n)$ reaction occurs when the excitation energy is 53.6 MeV. In this case, $\approx 77\%$ of the total xn cross section is observed in the $4n$ exit channel. The large uncertainties and small number of channels observed in the $^{44}\text{Ca} + ^{154}\text{Gd}$ reaction do not make a similar analysis meaningful for this target.

V. SUMMARY AND CONCLUSIONS

The $^{44}\text{Ca} + ^{154,156,157,160}\text{Gd}$ fusion-evaporation reactions have been studied for the first time. The peak $4n$ cross sections for the $^{157,160}\text{Gd}$ targets are on the order of a few millibarns, and the peak $4n$ cross sections for the $^{154,156}\text{Gd}$ reactions are on the order of tens to hundreds of microbarns. Combined

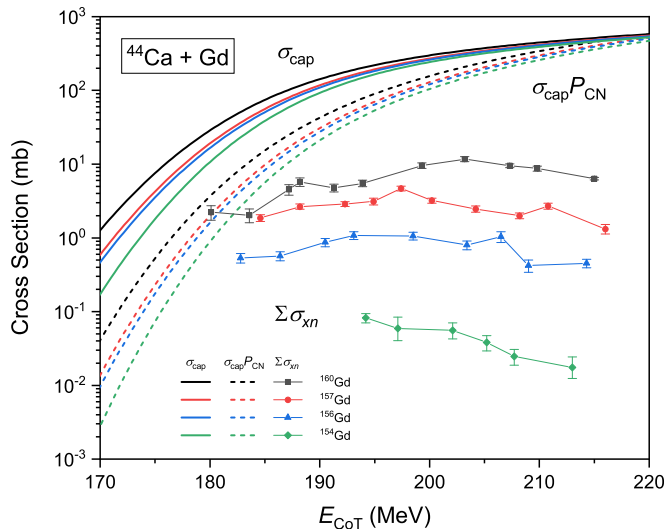


FIG. 5. Summary of cross section calculations and measurements. The heavy solid and dashed lines represent theoretical calculations of σ_{cap} and $\sigma_{\text{cap}}^{\text{P}_{\text{CN}}}$, respectively. The points connected by thin lines represent the sum of all measured xn channels in the current work. In all cases, the data series are in the same vertical order as the targets listed in the legend. See the main text for a discussion.

with our previous results on the $^{44}\text{Ca} + ^{158}\text{Gd}$ reaction, it appears that the peak $4n$ cross sections of the $^{44}\text{Ca} + ^{157,158,160}\text{Gd}$ reactions are all comparable in magnitude, and this may be due to relatively high values of $\overline{B}_f - \overline{S}_n$ for the relevant CN. In comparison, the peak $4n$ cross sections of the $^{44}\text{Ca} + ^{154,156}\text{Gd}$ reactions are notably smaller. The reaction with the most neutron-rich CN favored the $5n$ exit channel, the reaction with the most neutron-deficient CN favored the $3n$ channel, and other reactions favored the $4n$ channel. The most neutron-rich CN in this study has a reduced $4n$ cross section because a substantial fraction of its total xn cross section is contributing to higher exit channels. A theoretical model was employed to interpret the results, and it suggests that CELD is required in order to properly describe the experimental data, although $\overline{B}_f - \overline{S}_n$ is still the dominant factor in determining the final reaction cross section.

ACKNOWLEDGMENTS

The authors would like to thank the accelerator group and technical staff of the Cyclotron Institute for delivering the

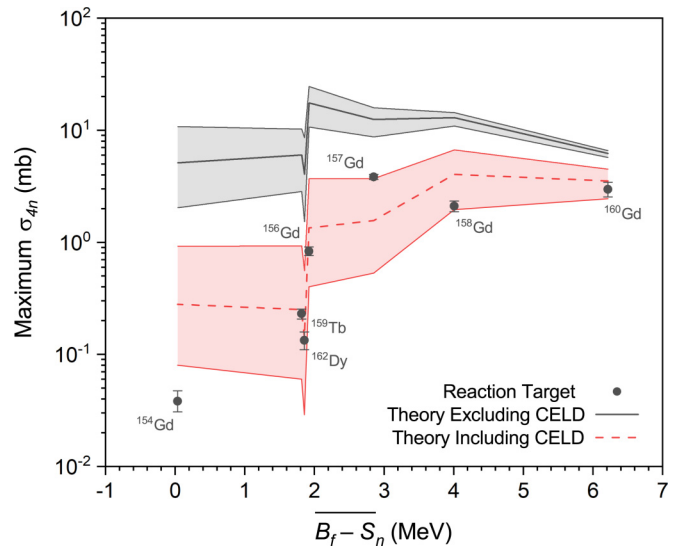


FIG. 6. Maximum $4n$ cross sections as a function of $\overline{B}_f - \overline{S}_n$ for reactions of ^{44}Ca projectiles with the indicated targets studied in the current work ($^{154,156,157,160}\text{Gd}$) and in our previous report (^{158}Gd , ^{159}Tb , and ^{162}Dy) [12]. Data points represent experimental data and lines represent theoretical calculations, which were only performed for the reactions indicated. The solid and dashed lines represent calculations excluding and including CELD, respectively. The shaded bands represent the effect of changing the fission barrier by ± 0.5 MeV in each case. The discontinuity in the theoretical calculations near $\overline{B}_f - \overline{S}_n \approx 2$ MeV is an artifact caused by the similar values of $\overline{B}_f - \overline{S}_n$ for the $^{44}\text{Ca} + ^{156}\text{Gd}$, ^{159}Tb , ^{162}Dy reactions. See the main text for a discussion.

beams of ^{44}Ca . We thank Prof. B. V. Miller in the Department of Geology & Geophysics at Texas A&M University, and separately the Center for Chemical Characterization and Analysis at Texas A&M University, for assistance with LA-ICP-MS. Use of the TAMU Materials Characterization Facility and Dr. Y. Bisrat and Dr. W. Serem are acknowledged for the EDS analyses. This material is based upon work supported by the U.S. Department of Energy, Office of Science, Office of Nuclear Physics under Award No. DE-FG02-93ER40773.

C.M.F. conceived of the experiment and served as principal investigator. All authors contributed to collecting the data. The analyses were conducted by T.A.W. and C.S.S. The manuscript text was written by T.A.W. and C.M.F., while T.A.W., C.M.F., K.J.G., and D.A.M. prepared the figures.

- [1] P. J. Karol, R. C. Barber, B. M. Sherrill, E. Vardaci, and T. Yamazaki, *Pure Appl. Chem.* **88**, 139 (2016).
- [2] P. J. Karol, R. C. Barber, B. M. Sherrill, E. Vardaci, and T. Yamazaki, *Pure Appl. Chem.* **88**, 155 (2016).
- [3] Yu. Ts. Oganessian and V. K. Utyonkov, *Rep. Prog. Phys.* **78**, 036301 (2015).
- [4] S. Hofmann *et al.*, *Eur. Phys. J. A* **52**, 180 (2016).
- [5] S. Hofmann *et al.*, Probing shell effects at $Z = 120$ and $N = 184$, in GSI Scientific Report 2008 (Darmstadt, Germany,

2009, unpublished), p. 131, available at <https://repository.gsi.de/record/53523/files/GSI-Report-2009-1.pdf>.

- [6] Yu. Ts. Oganessian *et al.*, *Phys. Rev. C* **79**, 024603 (2009).
- [7] J. Khuyagbaatar *et al.*, *Phys. Rev. C* **102**, 064602 (2020).
- [8] J. Khuyagbaatar *et al.*, The superheavy element search campaigns at TASCA, in GSI Scientific Report 2012 (Darmstadt, Germany, 2013, unpublished), p. 131, available at <http://repository.gsi.de/record/52034/files/PHN-ENNA-EXP-01.pdf>.

- [9] Ch. E. Düllmann *et al.*, Upgrade of the gas-filled recoil separator TASCA and first search experiment for the new element 120 in the reaction $^{50}\text{Ti} + ^{249}\text{Cf}$, in GSI Scientific Report 2011 (Darmstadt, Germany, 2012, unpublished), p. 206, available at http://www-win.gsi.de/tasca/publications/annual_reports/annual_reports_2011/PHN-NUSTAR-SHE-02.pdf.
- [10] V. K. Utyonkov *et al.*, *Phys. Rev. C* **92**, 034609 (2015).
- [11] K. Siwek-Wilczyńska, T. Cap, and J. Wilczyński, *Intl. J. Mod. Phys. E* **19**, 500 (2010).
- [12] T. A. Werke, D. A. Mayorov, M. C. Alfonso, E. E. Tereshatov, and C. M. Folden III, *Phys. Rev. C* **92**, 054617 (2015).
- [13] T. A. Werke, D. A. Mayorov, M. C. Alfonso, M. E. Bennett, M. J. DeVanzo, M. M. Frey, E. E. Tereshatov, and C. M. Folden III, *Phys. Rev. C* **92**, 034613 (2015).
- [14] D. A. Mayorov, T. A. Werke, M. C. Alfonso, E. E. Tereshatov, M. E. Bennett, M. M. Frey, and C. M. Folden III, *Phys. Rev. C* **92**, 054601 (2015).
- [15] D. A. Mayorov, T. A. Werke, M. C. Alfonso, M. E. Bennett, and C. M. Folden III, *Phys. Rev. C* **90**, 024602 (2014).
- [16] A. R. Jungmans, M. de Jong, H. G. Clerc, A. V. Ignatyuk, G. A. Kudyayev, and K. H. Schmidt, *Nucl. Phys. A* **629**, 635 (1998).
- [17] R. E. Tribble, R. H. Burch, and C. A. Gagliardi, *Nucl. Instrum. Methods Phys. Res. A* **285**, 441 (1989).
- [18] R. E. Tribble, C. A. Gagliardi, and W. Liu, *Nucl. Instrum. Methods Phys. Res. B* **56/57**, 956 (1991).
- [19] W. Parker and R. Falk, *Nucl. Instrum. Methods* **16**, 355 (1962).
- [20] W. Parker, H. Bildstein, N. Getoff, H. Fischer-Colbrie, and H. Regal, *Nucl. Instrum. Methods* **26**, 61 (1964).
- [21] D. A. Mayorov, E. E. Tereshatov, T. A. Werke, M. M. Frey, and C. M. Folden III, *Nucl. Instrum. Methods Phys. Res. B* **407**, 256 (2017).
- [22] T. A. Werke, Ph.D. thesis, Texas A&M University, 2016, available at <https://hdl.handle.net/1969.1/158028>.
- [23] E. Segrè, *Nuclei and Particles: An Introduction to Nuclear and Subnuclear Physics*, 2nd ed. (W. A. Benjamin, Reading, MA, 1977), pp. 26–27.
- [24] C. M. Folden III, M. C. Alfonso, D. A. Mayorov, K. R. Lawrence, A. A. Alharbi, E. Berdugo, P. J. Cammarata, A. C. Raphelt, B. T. Roeder, and T. A. Werke, *Nucl. Instrum. Methods Phys. Res. A* **678**, 1 (2012).
- [25] A. N. Andreev, D. D. Bogdanov, A. V. Eremin, A. P. Kabachenko, Yu. A. Muzychka, O. A. Orlova, B. I. Pustyl'nik, G. M. Ter-Akop'yan, V. I. Chepigin, and Sh. Sharo, *Sov. J. Nucl. Phys.* **52**, 412 (1990).
- [26] National Nuclear Data Center, available at <https://www.nndc.bnl.gov>.
- [27] V. I. Zagrebaev, A. S. Denikin, A. P. Alekseev, A. V. Karpov, V. V. Samarina, M. A. Naumenko, and A. Y. Kozhin, Computer Code EVAPORATION RESIDUES, available at <http://nrv.jinr.ru/nrv/>.
- [28] D. C. Radford, Computer Code RADWARE, available at <https://radware.phy.ornl.gov>.
- [29] W. J. Świątecki, K. Siwek-Wilczyńska, and J. Wilczyński, *Phys. Rev. C* **71**, 014602 (2005).
- [30] K. Siwek-Wilczyńska, A. Borowiec, I. Skwira-Chalot, and J. Wilczyński, *Intl. J. Mod. Phys. E* **17**, 12 (2008).
- [31] J. D. Jackson, *Can. J. Phys.* **34**, 767 (1956).
- [32] K. Siwek-Wilczyńska, I. Skwira, and J. Wilczyński, *Phys. Rev. C* **72**, 034605 (2005).
- [33] W. Reisdorf, *Z. Phys. A* **300**, 227 (1981).
- [34] A. V. Ignatyuk, G. N. Smirenkin, and A. S. Tishin, *Sov. J. Nucl. Phys.* **21**, 255 (1975).
- [35] A. J. Sierk, Computer Code FISROT, available at <https://www-nds.iaea.org/RIPL-3/fission/fis-barrier-liquiddrop.for>.
- [36] A. J. Sierk, *Phys. Rev. C* **33**, 2039 (1986).
- [37] P. Möller, A. J. Sierk, T. Ichikawa, and H. Sagawa, *At. Data Nucl. Data Tables* **109-110**, 1 (2016).
- [38] W. E. Parker *et al.*, *Phys. Rev. C* **44**, 774 (1991).
- [39] V. I. Zagrebaev, Y. Aritomo, M. G. Itkis, Yu. Ts. Oganessian, and M. Ohta, *Phys. Rev. C* **65**, 014607 (2001).
- [40] P. Möller, J. R. Nix, W. D. Myers, and W. J. Swiatecki, *At. Data Nucl. Data Tables* **59**, 185 (1995).
- [41] K.-H. Schmidt, C.-C. Sahn, K. Pielenz, and H.-G. Clerc, *Z. Phys. A* **316**, 19 (1984).
- [42] M. Shamsuzzoha Basunia, *Nucl. Data Sheets* **143**, 1 (2017).